



Title	Raman fingerprint for semi-metal WTe₂ evolving from bulk to monolayer
Author(s)	Jiang, YC; Gao, J; Wang, L
Citation	Scientific Reports, 2016, v. 6, p. 19624:1-7
Issued Date	2016
URL	http://hdl.handle.net/10722/223871
Rights	This work is licensed under a Creative Commons Attribution-NonCommercial-NoDerivatives 4.0 International License.

SCIENTIFIC REPORTS

OPEN

Raman fingerprint for semi-metal WTe_2 evolving from bulk to monolayer

Y. C. Jiang^{1,2}, J. Gao² & L. Wang^{2,3}

Received: 27 May 2015

Accepted: 14 December 2015

Published: 22 January 2016

Tungsten ditelluride (WTe_2), a layered transition-metal dichalcogenide (TMD), has recently demonstrated an extremely large magnetoresistance effect, which is unique among TMDs. This fascinating feature seems to be correlated with its special electronic structure. Here, we report the observation of 6 Raman peaks corresponding to the A_2^4 , A_1^9 , A_1^8 , A_1^6 , A_1^5 and A_1^2 phonons, from the 33 Raman-active modes predicted for WTe_2 . This provides direct evidence to distinguish the space group of WTe_2 from those of other TMDs. Moreover, the Raman evolution of WTe_2 from bulk to monolayer is clearly revealed. It is interesting to find that the A_2^4 mode, centered at $\sim 109.8 \text{ cm}^{-1}$, is forbidden in a monolayer, which may be attributable to the transition of the point group from C_{2v} (bulk) to C_{2h} (monolayer). Our work characterizes all observed Raman peaks in the bulk and few-layer samples and provides a route to study the physical properties of two-dimensional WTe_2 .

Transition-metal dichalcogenides (TMDs) of the MX_2 type, where M refers to Mo and W, and X refers to S, Se and Te, have attracted much attention as graphene-like semiconductors with remarkable electric, spintronic and optical properties^{1–7}. The basic structure of bulk MX_2 comprises two-dimensional (2D) X-M-X layers stacked through Van der Waals forces. Mono- and few-layer MX_2 can be fabricated by the mechanical exfoliation method⁸. The physical properties of MX_2 are greatly dependent on the number of layers^{9–11}. Weak Van der Waals forces play a very important role in the interlayer bands and atomic vibration. As the thickness decreases, MX_2 exhibits a transition from indirect to direct gaps, while the frequency of the Raman peaks shift away from those of the bulk sample^{12,13}.

Tungsten ditelluride (WTe_2) is a unique TMD as it has the large interlayer spacing, an orthorhombic lattice structure and a semi-metal electronic structure^{1,14–16}. This material has drawn extensive interest since the recent discovery of an extremely large magnetoresistance (XMR) effect in diamagnetic WTe_2 single crystal, which has not been observed in other TMDs¹. Such a fascinating feature implies potential spintronic applications for mono- and few-layer WTe_2 . However, to date no study has examined the physical properties of the 2D WTe_2 system. Raman spectroscopy is a powerful tool for investigating the symmetries of 2D semiconductors; it is necessary, therefore, to characterize the Raman fingerprint of WTe_2 as it evolves from a 3D to a 2D system.

This article reports the observation of Raman scattering in bulk and few-layer WTe_2 samples. Six optical vibrational modes, A_2^4 , A_1^9 , A_1^8 , A_1^6 , A_1^5 and A_1^2 , were observed at room temperature. Density functional perturbation theory (DFPT) was used to calculate phonon branches, simulate Raman spectra and verify their corresponding optical phonons. Group analysis demonstrated that the lattice symmetry differentiated WTe_2 from other TMDs^{17,18}. In our experiments, WTe_2 flakes, exfoliated from a piece of bulk, showed strong thickness-dependent Raman spectra. As the number of layers increased, the A_1^8 and A_1^2 modes softened (red-shift) and the A_2^4 and A_1^5 mode stiffened (blue-shift). It was also interesting to find that the A_2^4 mode was absent in the monolayer. This phenomenon may be attributable to the transition of the point group from C_{2v} to C_{2h} . Our results provide a well-defined and reliable method for determining the number of layers using Raman spectroscopy.

¹Research Center for Solid State Physics and Materials, School of Mathematics and Physics, Suzhou University of Science and Technology, Suzhou 215009, China. ²Department of Physics, The University of Hong Kong, Pokfulam Road, Hong Kong. ³School of Materials Science and Engineering, Shanghai University, 333 Nanchen Road, Baoshan District, Shanghai 200444, China. Correspondence and requests for materials should be addressed to J.G. (email: jugao@hku.hk)

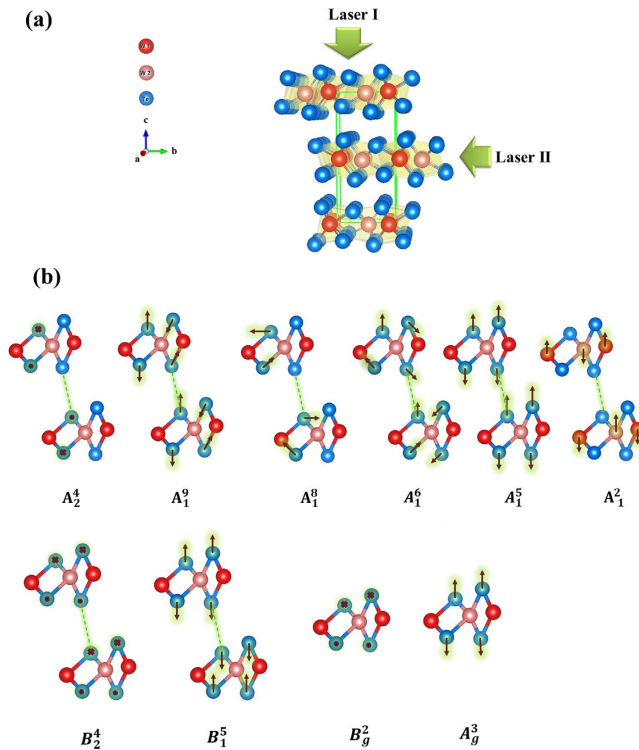


Figure 1. Lattice structure. (a) Crystal structure of WTe_2 along the a -axis direction, showing the orthorhombic unit cell. (b) Atomic displacements of Raman active modes in WTe_2 bulk and monolayer. Here, “ \times ” and “ \cdot ” indicate that the Te atoms move into and out of the bc plane, respectively.

Results and Discussions

Figure 1a shows the layered crystal structure of WTe_2 , in which tungsten layers are sandwiched between two neighboring tellurium sheets. The distance (0.703 nm) between two adjacent sandwich layers is the largest of all known TMDs. Most TMDs exhibit a hexagonal structure with the space group D^4_{6h} . However, naturally formed WTe_2 reveals an orthorhombic unit cell with the space group C^7_{2v} ($Pmn2_1$), which may be derived from a distorted hexagonal net^{1,15}. The unit cell contains two tungsten atoms and four tellurium atoms. The two tungsten atoms (distinguished by W1 and W2) are not equivalent to each other and the W-Te bond length ranges from 2.7 to 2.8 Å. WTe_2 bulk exhibits the T_d stacking order, in which the atoms in the upper layer are rotated by 180 degrees with respect to those in the lower layer¹⁷. And the tungsten atoms shift away from the center of the octahedron formed by the tellurium atoms. Therefore, the vibrational modes of WTe_2 are very different from those of 2H-MX_2 , and the previous calculation of vibrational modes, based on 2H-WTe_2 , is inapplicable to our experimental Raman results¹⁹.

Due to the C^7_{2v} symmetry group, the irreducible representations of the optical phonons in the bulk WTe_2 at the center of the Brillouin zone (Γ point) are

$$\Gamma_{\text{bulk}} = 11A_1 + 6A_2 + 11B_1 + 5B_2, \quad (1)$$

where all of the vibrational modes are Raman active, and the $11A_1$, $11B_1$ and $5B_2$ modes are infrared active. Here, the Raman tensors corresponding to different symmetries can be written as

$$\alpha(A_1) = \begin{pmatrix} a & 0 & 0 \\ 0 & b & 0 \\ 0 & 0 & c \end{pmatrix}, \quad \alpha(A_2) = \begin{pmatrix} 0 & d & 0 \\ d & 0 & 0 \\ 0 & 0 & 0 \end{pmatrix},$$

$$\alpha(B_1) = \begin{pmatrix} 0 & 0 & 0 \\ 0 & 0 & e \\ 0 & e & 0 \end{pmatrix}, \quad \alpha(B_2) = \begin{pmatrix} 0 & 0 & f \\ 0 & 0 & 0 \\ f & 0 & 0 \end{pmatrix}. \quad (2)$$

Although 33 Raman vibrations are predicted by group theory, only 6 Raman peaks were observed in our experiments. To distinguish these vibrational modes, we use Z_m^n ($Z = A$ or B ; $m = 1$ or 2 ; $n = \text{integer}$) to represent them. The frequency of Z_m^n mode is smaller than that of Z_m^l mode if n is larger than l . This method allows us to name all appropriate vibrational modes.

DFPT has been used to calculate all 33 Raman vibrational modes. Among them, the atomic displacements of the six Raman active modes that could potentially explain our Raman results are shown in Fig. 1b. The Raman spectra of WTe_2 bulk at room temperature are presented in Fig. 2a. Raman peaks centered at $\sim 109.8 \text{ cm}^{-1}$,

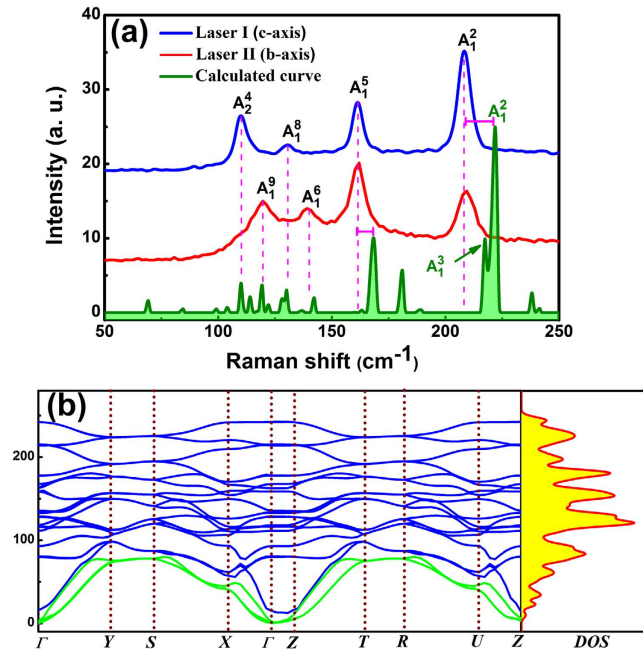


Figure 2. Experimental and calculated phonons. (a) Raman spectra of the bulk sample with incident Laser I and Laser II along the *c*- and *b*-axes at room temperature, respectively. The calculated Raman spectrum is plotted for comparison. (b) Calculated phonon dispersion curve along the Γ -Y-X- Γ -Z direction in the orthorhombic Brillouin zone (BZ), and the vibrational density of states (DOS) for WTe₂ bulk at the equilibrium volume. The blue and green curves are the optical and acoustic vibrational branches, respectively.

$\sim 130.4 \text{ cm}^{-1}$, $\sim 162.5 \text{ cm}^{-1}$ and 208.4 cm^{-1} were observed with Laser I applied in the $z(xx)\bar{z}$ geometry. Another two Raman peaks, centered at $\sim 119.6 \text{ cm}^{-1}$ and $\sim 139.1 \text{ cm}^{-1}$, were observed with Laser II applied in the $y(zz)\bar{y}$ geometry. Due to the non-polarized Raman measurement, the \vec{e}_i and \vec{e}_s vectors are not along *a*- or *c*-axis in the either geometry. Thus, a total of six Raman peaks were identified in our experiments. Due to the non-polarized Raman measurements, the assignment of these Raman peaks could not be performed through symmetry analysis. Instead, we calculated the Raman intensities and spectrum (green curve in Fig. 2a) to verify the phonon modes corresponding to the observed Raman peaks. Only 6 Raman peaks were observed in comparison with 33 Raman modes in theory, which suggests that only those modes with high Raman intensities might appear experimentally. For example, Table 1 shows that for the first Raman peak (centered at $\sim 109.8 \text{ cm}^{-1}$), the A_2^4 , A_2^5 and B_2^4 modes were all candidates, with frequencies close to $\sim 110 \text{ cm}^{-1}$. Only the A_2^4 mode exhibited a sufficiently strong Raman intensity, whereas the intensities of the others were very weak. Therefore, the A_2^4 mode should be assigned to the first peak. Similarly, the A_1^9 ($\sim 119.6 \text{ cm}^{-1}$), A_1^8 ($\sim 130.4 \text{ cm}^{-1}$), A_1^6 ($\sim 139.1 \text{ cm}^{-1}$), A_1^5 ($\sim 162.5 \text{ cm}^{-1}$) and A_1^2 ($\sim 208.4 \text{ cm}^{-1}$) modes were assigned frequencies from low to high, which agrees with the results in ref. 20. It should be noted that although the A_1^2 mode was associated with the peak centered at $\sim 208.4 \text{ cm}^{-1}$, the A_1^3 mode still exhibited a strong Raman intensity theoretically and could not be neglected. It is very possible that the A_1^2 and A_1^3 modes both exist, but the difference between their frequencies is so small that they cannot be distinguished in the Raman spectra.

As shown in Fig. 1b, the first five modes originate from the relative movements of Te atoms, while the A_1^2 mode is due to the displacement between adjacent W1 and W2 atoms. A_2^4 and A_1^5 are pure longitudinal and transverse optical modes, respectively. For the in-plane configuration $[z(xx)\bar{z}]$, the B_1 and B_2 modes are forbidden due to the forms of their Raman tensors. In the case of the out-of-plane configuration $[y(zz)\bar{y}]$, the A_2^4 mode may be forbidden and the A_1^8 Raman intensity vanishes. Instead, the A_1^6 and A_1^9 modes reveal significant Raman intensities. Here when we state that one mode is “forbidden”, it means that this Raman mode is prevented from observing by group theory or unable to exist on account of the DFPT calculation, while “vanish” means a Raman mode is active in theory, but in a certain configuration its intensity is too weak to observe due to the specific parameters in its Raman tensor. To clarify this phenomenon, the relationship between Raman intensity and Raman tensor can be written as²¹

$$I = [e_s \alpha e_i]^2 |E_0|^2, \quad (3)$$

where e_s and e_i are the scattered light and incident light vectors, respectively. This equation makes it easy to understand the anisotropy of the A_2^4 mode. The specific values of *a*, *b* and *c* in the Raman tensors of the A_1^8 , A_1^6 and A_1^9 modes determine the dependence on the laser configuration. In the case of Laser I, the A_1^6 and A_1^9 modes with very small values of *a* and *b* vanish, while the A_1^8 mode appears due to its large value of *b*. There is a similar effect for Laser II: the A_1^6 and A_1^9 modes appear due to their large *c* values and the A_1^8 mode vanishes due to its very

Symmetry	Raman Activity	Infrared Activity	Experimental Frequency (cm ⁻¹)	Calculated Frequency (cm ⁻¹)
A ₁ ¹¹	Y	Y		10.9
B ₁ ¹¹	Y	Y		23.9
A ₂ ⁶	Y	N		29.7
A ₁ ¹⁰	Y	Y		69.3
B ₁ ¹⁰	Y	Y		84.8
B ₂ ⁵	Y	Y		99.3
A ₂ ⁵	Y	N		103.9
A ₂ ⁴	Y	N	109.8	110.0
B ₂ ⁴	Y	Y		112.5
A ₂ ³	Y	N		114.0
B ₂ ³	Y	Y		117.4
A ₁ ⁹	Y	Y	119.6	119.4
B ₁ ⁹	Y	Y		122.1
B ₁ ⁸	Y	Y		127.9
B ₁ ⁷	Y	Y		129.5
A ₁ ⁸	Y	Y	130.4	130.0
A ₁ ⁷	Y	Y		136.0
B ₁ ⁶	Y	Y		137.3
A ₁ ⁶	Y	Y	139.1	142.3
A ₂ ²	Y	N		160.0
B ₂ ²	Y	Y		160.1
B ₁ ⁵	Y	Y		163.3
A ₁ ⁵	Y	Y	162.5	168.5
A ₂ ¹	Y	N		180.1
B ₂ ¹	Y	Y		181.2
B ₁ ⁴	Y	Y		188.6
A ₁ ⁴	Y	Y		189.7
A ₁ ³	Y	Y		217.3
B ₁ ³	Y	Y		218.1
A ₁ ²	Y	Y	208.4	222.2
B ₁ ²	Y	Y		223.1
B ₁ ¹	Y	Y		238.1
A ₁ ¹	Y	Y		241.7

Table 1. All of the possible optical phonons investigated through calculations and experiments. “Y” or “N” indicates that the chosen mode is allowed or forbidden.

small a and c values. The a, b and c values of the A₁² and A₁⁵ modes are large enough for them to be observed in both configurations.

Figure 2b shows the calculated phonon dispersion curve in the Brillouin zone and the density of states for the WTe₂ bulk. There are 3 acoustic (green curves) and 33 optical (blue curves) phonon branches. Table 1 shows all of the calculated and experimental vibrational modes. The calculated Raman intensities of the A₂⁴, A₁⁹, A₁⁸, A₁⁶, A₁⁵ and A₁² modes are strong at frequencies of ~110.0 cm⁻¹, ~119.4 cm⁻¹, ~130.0 cm⁻¹, ~142.3 cm⁻¹, ~168.5 cm⁻¹ and 222.2 cm⁻¹, respectively. The good agreement between the experimental and theoretical results supports our assignment of the Raman vibrational modes. It should be noted that all calculations were performed at zero temperature, while the Raman spectra were investigated at room temperature. Although frequencies of phonon modes depend on the temperature, it is unable to influence the assignment of the Raman modes. The frequency displacements between 5 K and 294 K were less than 4 cm⁻¹ for all of the observed Raman peaks²⁰. Such small displacements would not affect the association with specific phonon modes. In addition, the frequencies of all Raman peaks increase as the temperature increases, which may explain why most of the calculated frequencies were higher than those measured in the experiments.

WTe₂ flakes were fabricated on a Si substrate with a 300 nm SiO₂ layer using the mechanical exfoliation method. As shown in Fig. 3a,b, an ultrathin WTe₂ flakes was first identified by optical microscopy, and then imaged by atomic force microscopy (AFM) to determine its thickness. Figure 3c shows that the height of a monolayer WTe₂ on the SiO₂ layer is about 1.1 nm, while the height of the monolayer on the WTe₂ flake is 0.7~0.9 nm and close to the interlayer spacing (about 0.703 nm) of the bulk.

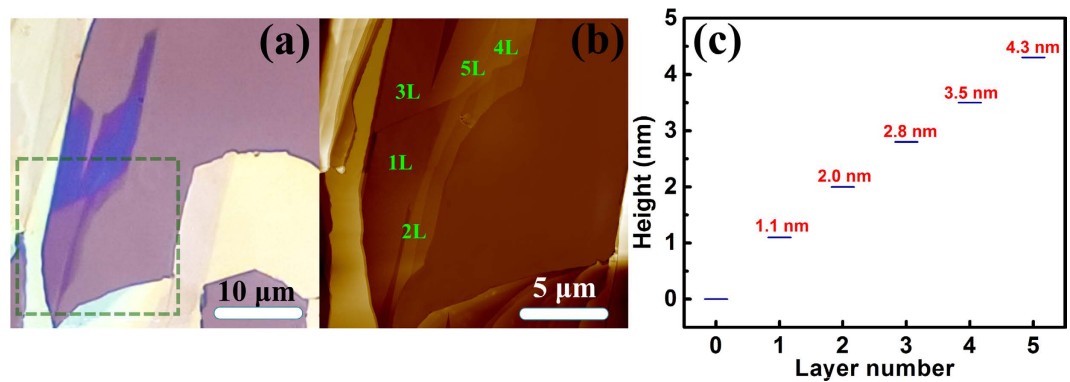


Figure 3. Microscopic Imaging. (a) Optical microscopic images of mono- to multilayer WTe₂ on a Si substrate with a 300 nm SiO₂ layer. (b) AFM image of the area (20 × 20 μm²) surrounded by a green dashed line in (a). (c) Height of the flake as a function of the layer number.

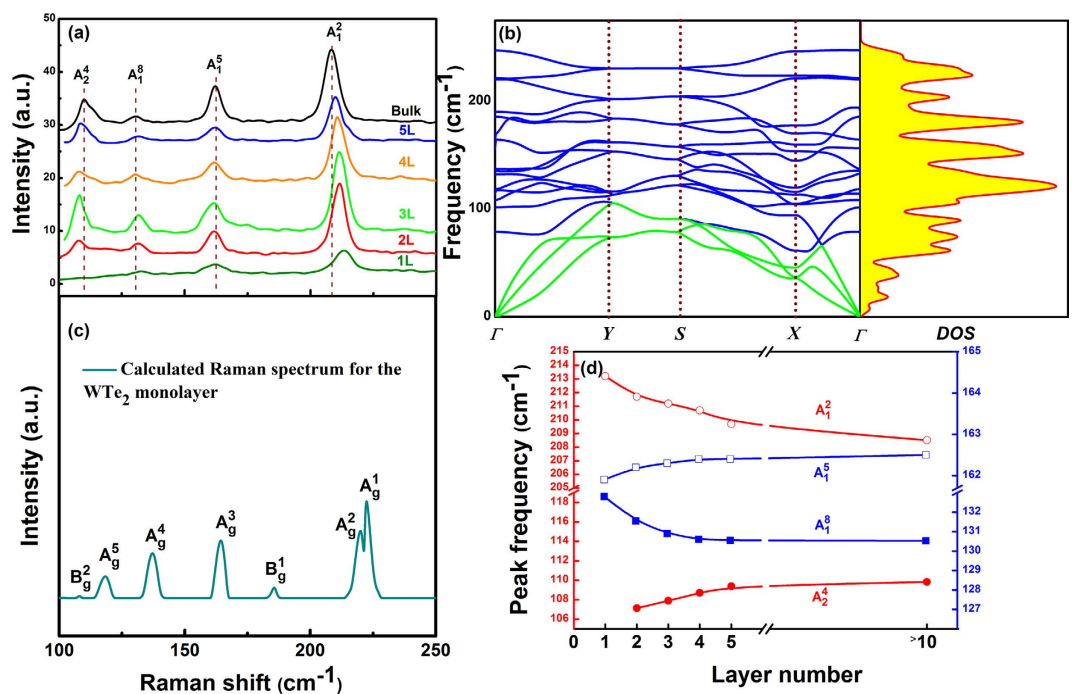


Figure 4. Raman evolution. (a) Raman spectra of bulk and few-layer WTe₂. (b) Calculated phonon dispersion curve along the Γ -Y-X- Γ direction in the orthorhombic BZ, and DOS for the WTe₂ monolayer. Blue and green curves are optical and acoustic vibrational branches, respectively. (c) Calculated Raman spectrum for the WTe₂ monolayer. (d) Frequencies of the A₂⁴, A₁⁸, A₁⁵ and A₁² modes as functions of the layer number.

Figure 4a illustrates the Raman spectra of WTe₂ as it evolved from bulk to monolayer. The four Raman active modes can be observed in the 2L, 3L, 4L and 5L samples. It is interesting to note that the A₂⁴ mode is absent in the 1L sample, which may make it convenient to use the Raman spectra to identify the WTe₂ monolayer. The frequency difference between the A₂⁴ modes of the 2L sample and the bulk is about 2.7 cm⁻¹. The A₂⁴ and A₁⁸ modes stiffen (blue-shift) in frequency as the number of layers increases, while the A₁⁵ and A₁² modes soften (red-shift). The A₁⁵ mode is the most stable and the displacement of its Raman shift, caused by the change in thickness, is less than 1 cm⁻¹. In contrast, the A₁² mode is found to be the most sensitive to the number of layers, and shifts up by about 4.8 cm⁻¹ when the number of layers decreases to one.

With WTe₂ evolving from bulk to monolayer, its point group changes from C_{2v} to C_{2h}. The irreducible representation of the optical phonons in a WTe₂ monolayer at the Brillion zone center (Γ point) is expressed as:

$$\Gamma_{\text{monolayer}} = 6A_g + 2A_u + 3B_g + 4B_u, \quad (4)$$

Symmetry	Symmetry (bulk)	Experimental Frequency (cm ⁻¹)	Calculated Frequency (cm ⁻¹)
A_g^6	A_1^{10} or B_1^{10}		81.4
B_g^3	A_2^5 or B_2^5		93.2
B_g^2	B_2^4		108.5
A_u^2	A_2^3 or B_2^3		114.3
A_g^5	A_1^9		118.5
B_u^4	B_1^8		132.2
B_u^3	A_1^7 or B_1^7		135.1
A_g^4	A_1^8 or B_1^6 B_1^7	132.8	137.2
A_u^1	A_2^2 or B_2^2		156.6
A_g^3	A_1^5 or B_1^5	161.9	164.5
B_g^1	A_2^1 or B_2^1		185.7
B_u^2	A_1^4 or B_1^4		190.2
A_g^2	A_1^3		220.3
A_g^1	A_1^2	213.2	222.6
B_u^1	A_1^1 or B_1^1		247.2

Table 2. The calculated vibrational modes of the WTe₂ monolayer.

where A_g and B_g are Raman active; A_u and B_u are infrared active. Only nine Raman-active modes are allowed in the WTe₂ monolayer. This implies that some Raman peaks, observed in bulk, may be forbidden in the monolayer. Based on the group analysis, we calculated phonon dispersion curve in BZ, and DOS for WTe₂ monolayer as shown in Fig. 4b. There are three acoustic (green curves) and fifteen optical (blue curves) phonon branches.

The vibrational modes of the WTe₂ monolayer are exhibited in Table 2. To compare the vibrational modes of the bulk with those of the monolayer, we used the symmetry symbols of the C_{2v} and C_{2h} groups to name the corresponding modes, respectively. The atomic displacements of the Raman active modes were used to build a bridge between Raman modes of monolayer and bulk WTe₂ as shown in Fig. 1b. Two of the vibrational modes in the bulk may correspond to the same modes in the monolayer. For example, the A_1^5 and B_1^5 modes correspond to the A_g^3 mode in Table 2, indicating that the A_1^5 and B_1^5 modes have the same atomic displacement as that of the A_g^3 mode. For the A_1^5 mode, the upper and lower atom layers exhibit the same phase of the atomic oscillations. But for the B_1^5 mode, the upper atom layer has an anti-phase with respect to the lower atom layer. Both of the modes can be distinguished in the multilayer samples (layer number ≥ 2), but turn into the A_g^3 mode in the monolayer.

Our calculations show the A_2^4 mode is forbidden in the monolayer, which consists with the experiments. Figure 4c shows the calculated Raman spectrum of the WTe₂ monolayer. Only the B_g^2 mode is a candidate to correspond to the A_2^4 mode. However, Fig. 1b demonstrates that the atomic displacement of the B_g^2 mode is different from that of the A_2^4 mode, but the same as that of the B_2^4 mode. Therefore, the B_g^2 mode corresponds to the B_2^4 mode instead of the A_2^4 mode. On the basis of the theoretical analysis, the transition of point group from C_{2v} (bulk) to C_{2h} (monolayer) may be responsible for the absence of the A_2^4 mode. In addition, the atomic displacement of the A_2^4 mode shows that only the half of tellurium atoms participate in oscillation, while the other half remains still (see Fig. 1b). In contrast to WTe₂ bulk, all of the tellurium atoms participated in oscillation in the monolayer. This phenomenon may be attributed to the interlayer Van der Waals forces which are a dominant interaction between the adjacent atom layers. The loss of Van der Waals forces in the monolayer caused its atomic displacements to differ from those of bulk.

The frequencies of the four modes as a function of the number of layers are shown in Fig. 4d. The A_1^5 and A_2^4 modes stiffen and the A_1^8 , and A_1^2 modes soften as the WTe₂ monolayer evolves into a bulk. This implies that not only the interlayer Van der Waals coupling, but also stacking-induced structural changes or long-ranged Coulombic interlayer interaction may affect the atomic vibration^{9,22}. If only Van der Waals coupling influenced the atomic vibrations, the A_1^5 , A_2^4 , A_1^8 and A_1^2 modes should all stiffen with layer number increasing^{10,23}. The softening of the A_1^8 , and A_1^2 modes indicates that stacking-induced structural changes or long-ranged Coulombic interlayer interaction also plays an important role in the atomic vibration^{9,10,22}. Our calculated results for the WTe₂ monolayer confirm the shift directions of these vibrational modes.

In summary, we studied bulk and few-layer WTe₂ using Raman spectroscopy. The six first-order Raman-active modes observed at room temperature differed from those of all other TMDs. DFPT and group theory were used to analyze the frequencies of the Raman peaks and their corresponding vibration modes. The Raman peaks were found to correlate with the optical phonons of A_2^4 , A_1^9 , A_1^8 , A_1^6 , A_1^5 and A_1^2 . The A_2^4 mode was forbidden in the monolayer due to the transition of the point group from C_{2v} (bulk) to C_{2h} (monolayer). As the number of layers increased, the A_1^8 , and A_1^2 modes softened and the A_2^4 and A_1^5 modes stiffened. Our study characterized all of the Raman peaks observed in bulk and few-layer WTe₂ and provides a route to study the physical properties of 2D WTe₂.

Methods

The WTe₂ single crystals were prepared using a chemical vapor transport method described by ref. 1. WTe₂ flakes were mechanically exfoliated from a piece of bulk single crystal onto Si wafers covered with a 300-nm-thick SiO₂ layer. The few-layer samples were first identified by optical microscopy, and then measured by atomic-force microscopy (AFM) to determine the thickness. Micro-Raman spectroscopy was used to analyze the WTe₂ under ambient conditions. Non-polarized and off-resonance Raman measurements were performed with a 514.5-nm excitation laser. When the WTe₂ flakes were investigated, the power of the excitation laser was reduced to 0.5 mW to obtain reliable Raman spectra against the oxidation. Our calculation and analysis were performed on basis of DFPT and group theory, using the experimental lattice parameters $a = 3.496 \text{ \AA}$, $b = 6.282 \text{ \AA}$ and $c = 14.07 \text{ \AA}$ and the same wavelength of the incident light as that in experiments¹⁴. The exchange correlation potential was represented by the local density approximation (LDA). The Brillouin zone integrations were performed with a $16 \times 8 \times 4$ Monkhorst-Pack k-point mesh by using a plane-wave energy cutoff of 500 eV. All DFPT calculations model was appropriate for explaining the Raman spectrum using the CASTEP code²⁴.

References

1. Ali, M. N. *et al.* Large, non-saturating magnetoresistance in WTe₂. *Nature* **514**, 205–208 (2014).
2. Radisavljevic, B., Radenovic, A., Brivio, J., Giacometti, V. & Kis, A. Single-layer MoS₂ transistors. *Nat. Nano.* **6**, 147–150 (2011).
3. Coleman, J. N. *et al.* Two-dimensional nanosheets produced by liquid exfoliation of layered materials. *Science* **331**, 568–571 (2011).
4. Geim, A. K. & Grigorieva, I. V. Van der Waals heterostructures. *Nature* **499**, 419–425 (2013).
5. Gong, Y. *et al.* Vertical and in-plane heterostructures from WS₂/MoS₂ monolayers. *Nat. Mater.* **13**, 1135–1142 (2014).
6. Zeng, H., Dai, J., Yao, W., Xiao, D. & Cui, X. Valley polarization in MoS₂ monolayers by optical pumping. *Nat. Nano.* **7**, 490–493 (2012).
7. Zeng, H. *et al.* Optical signature of symmetry variations and spin-valley coupling in atomically thin tungsten dichalcogenides. *Sci. Rep.* **3**, 1608 (2013).
8. Novoselov, K. S. *et al.* Two-dimensional atomic crystals. *Proc. Natl. Acad. Sci. USA* **102**, 10451–10453 (2005).
9. Lee, C. *et al.* Anomalous Lattice Vibrations of Single- and Few-Layer MoS₂. *ACS Nano* **4**, 2695–2700 (2010).
10. Li, H. *et al.* From Bulk to Monolayer MoS₂: Evolution of Raman Scattering. *Adv. Funct. Mater.* **22**, 1385–1390 (2012).
11. Yamamoto, M. *et al.* Strong Enhancement of Raman Scattering from a Bulk-Inactive Vibrational Mode in Few-Layer MoTe₂. *ACS Nano* **8**, 3895–3903 (2014).
12. Mak, K. F., Lee, C., Hone, J., Shan, J. & Heinz, T. F. Atomically Thin MoS₂: A New Direct-Gap Semiconductor. *Phys. Rev. Lett.* **105**, 136805 (2010).
13. Splendiani, A. *et al.* Emerging Photoluminescence in Monolayer MoS₂. *Nano Lett.* **10**, 1271–1275 (2010).
14. Brown, B. The crystal structures of WTe₂ and high-temperature MoTe₂. *Acta Cryst.* **20**, 268–274 (1966).
15. Mar, A., Jobic, S. & Ibers, J. A. Metal-metal vs tellurium-tellurium bonding in WTe₂ and its ternary variants TaIrTe₄ and NbIrTe₄. *J. Am. Chem. Soc.* **114**, 8963–8971 (1992).
16. Kabashima, S. Electrical Properties of Tungsten-Ditelluride WTe₂. *J. Phys. Soc. Jpn.* **21**, 945–948 (1966).
17. Augustin, J. *et al.* Electronic band structure of the layered compound Td-WTe₂. *Phys. Rev. B* **62**, 10812–10823 (2000).
18. Rousseau, D. L., Bauman, R. P. & Porto, S. P. S. Normal mode determination in crystals. *J. Raman Spectrosc.* **10**, 253–290 (1981).
19. Ataca, C., Şahin, H. & Ciraci, S. Stable, Single-Layer MX₂ Transition-Metal Oxides and Dichalcogenides in a Honeycomb-Like Structure. *J. Phys. Chem. C* **116**, 8983–8999 (2012).
20. Kong, W.-D. *et al.* Raman scattering investigation of large positive magnetoresistance material WTe₂. *Appl. Phys. Lett.* **106**, 081906 (2015).
21. Bower, D. I. Investigation of Molecular Orientation Distributions by Polarized Raman Scattering and Polarized Fluorescence. *J. Polym. Sci. Polym. Phys. Ed.* **10**, 2135–2153 (1972).
22. Wieting, T. J. & Verble, J. L. Interlayer Bonding and the Lattice Vibrations of β-GaSe. *Phys. Rev. B* **5**, 1473–1479 (1972).
23. Bagnall, A. G., Liang, W. Y., Marseglia, E. A. & Welber, B. Raman studies of MoS₂ at high pressure. *Physica* **99B**, 343 (1980).
24. Clark, S. J. *et al.* First principles methods using CASTEP. *Z. Kristallogr* **220**, 567 (2005).

Acknowledgements

The authors thank Dr. An Zhao, Dr. Bairen Zhu and Dr. Xiangbo Liu for their fruitful discussions, and Miss Manxiu Feng for her technique support. This work has been supported by the National Key Project for Basic Research (No. 2014CB921002), the National Natural Science Foundation of China (Grant No. 11504254, 11374225, 11574227, 11304193), and the Research Grant Council of Hong Kong (Project code: 701813). This work is also supported by the Priority Academic Program Development of Jiangsu Higher Education Institutions and the USTS Cooperative Innovation Center for Functional Oxide Films and Optical Information.

Author Contributions

J.G. proposed and led the project. Y.C.J. designed and did all the experiments. Y.C.J. and L.W. performed the DFPT calculations. Y.C.J. and J.G. wrote the manuscript and prepared all figures together.

Additional Information

Competing financial interests: The authors declare no competing financial interests.

How to cite this article: Jiang, Y. C. *et al.* Raman fingerprint for semi-metal WTe₂ evolving from bulk to monolayer. *Sci. Rep.* **6**, 19624; doi: 10.1038/srep19624 (2016).



This work is licensed under a Creative Commons Attribution 4.0 International License. The images or other third party material in this article are included in the article's Creative Commons license, unless indicated otherwise in the credit line; if the material is not included under the Creative Commons license, users will need to obtain permission from the license holder to reproduce the material. To view a copy of this license, visit <http://creativecommons.org/licenses/by/4.0/>